CHEMISTRY OF MATERIALS

Article

Influence of the Arrangement of the Octahedrally Coordinated Trivalent Cobalt Cations on the Electrical Charge Transport and Surface Reactivity

Patrick Herve Tchoua Ngamou and Naoufal Bahlawane*

Department of Chemistry, Bielefeld University, Universitaetsstr. 25, 33615 Bielefeld, Germany

Received February 13, 2010. Revised Manuscript Received May 28, 2010

The spinel (Co_3O_4) and the perovskite ($LaCoO_3$) oxides are two distinct structures that have in common the trivalent cobalt cations in the octahedral sublattice but in contrasting interconnection geometries. Several properties are directly related to these octahedra, which are edge-connected in the spinel and vertex-connected in the perovskite structure. The electrical charge transport was investigated in both materials to explain the superior conductivity of the perovskite despite the confirmed high mobility barrier. The surface probing indicates the higher reducibility of the spinel, and higher abundance and strength of the basic sites in the perovskite structure. The consequence of the contrasting physicochemical properties of these two materials, edge- and vertex-connected octahedra, on the surface reactivity was discussed in terms of the catalytic efficiency toward the oxidation of CO, aromatics, and alcohols.

1. Introduction

Among the 3d transition-metal oxides, those containing cobalt such as spinel Co_3O_4 and perovskite $LaCoO_3$ structures are of interest in several fields of applied technology. For instance, due to their electrical conductivity, Co_3O_4-based materials have been investigated as gas sensors,[1] electrocatalysts,[2] and electrodes for lithium ion batteries,[3] while $LaCoO_3$-based materials are used as cathodes in solid oxide fuel cells (SOFC)[4] and gas sensors.[5] $LaCoO_3$ and Co_3O_4 materials were also studied with a focus on their magnetic[6,7] and catalytic properties.[8-11] The spinel Co_3O_4, $(Co^{2+})[Co^{3+}]_2O_4$, belongs to a class of complex oxides where Co^{2+} cations occupy the tetrahedral sites and Co^{3+} cations are located in octahedral sites, while in the perovskite $LaCoO_3$, $(La^{3+})[Co^{3+}]O_3$, Co^{3+} cations are located in the octahedral and La^{3+} in the cuboctahedral sites. The presence of trivalent cobalt cations in the octahedral sites plays a pivotal role in the electrical and catalytic properties. A fraction of Co^{3+} cations undergoes a charge disproportionation and leads to the formation of tetravalent cobalt cations (Co^{4+}) that are the carriers (holes) of the electrical charge.[12-16] Furthermore, the presence of the tetravalent cobalt cations at the surface of the oxide promotes the adsorption of oxygen and consequently increases the surface basicity of the material.[17,18] The catalytic performance of $LaCoO_3$ and Co_3O_4 toward the deep oxidation of hydrocarbons is related to their redox properties that are controlled by the ability of reducing the Co^{3+} cations.[8,19] In spite of the intensively investigated role of the octahedrally coordinated trivalent cobalt cation, little concerns were given to the effect of the structural arrangement of these octahedra. In fact, in the spinel Co_3O_4 structure, neighboring octahedral sites share their edges, while they share their vertexes in the perovskite structure. This structural detail, which is supposed to influence the charge transport and the surface reactivity of these materials, is experimentally investigated in this study.

*To whom correspondence should be addressed. Tel: +49(0)521 106 2199. Fax: +49(0)521 106 6027. E-mail: naoufal@pc1.uni-bielefeld.de.

 (1) Chaudhari, G. N.; Pawar, M. J. *J. Optoelect. Adv. Mater.* **2008**, *10* (10), 2574–2577.
 (2) Laouini, E.; Hamdani, M.; Pereira, M. I. S.; Douch, J.; Mendonca, M. H.; Berghoute, Y.; Singh, R. N. *Int. J. Hydrogen Energy* **2008**, *33*(19), 4936–4944.
 (3) Lavela, P.; Tirado, J. L.; Vidal-Abarca, C. *Electrochim. Acta* **2007**, *52*(28), 7986–7995.
 (4) Srdic, V. V.; Omorjan, R. P.; Seydel, J. *Mater. Sci. Eng., B* **2005**, *116*(2), 119–124.
 (5) Ajami, S.; Mortazavi, Y.; Khodadadi, A.; Pourfayaz, F.; Mohajerzadeh, S. *Sens. Actuators B* **2006**, *117*(2), 420–425.
 (6) Baskar, D.; Adler, S. B. *Chem. Mater.* **2008**, *20*(8), 2624–2628.
 (7) Kim, K. J.; Kim, H. K.; Park, Y. R.; Ahn, G. Y.; Kim, C. S.; Park, J. Y. *J. Magn. Magn. Mater.* **2006**, *300*(2), 300–305.
 (8) Bahlawane, N. *Appl. Catal., B* **2006**, *67*(3−4), 168–176.
 (9) Bahlawane, N.; Rivera, E. F.; Kohse-Hoinghaus, K.; Brechling, A.; Kleineberg, U. *Appl. Catal., B* **2004**, *53*(4), 245–255.
(10) Tian, Z. Y.; Bahlawane, N.; Qi, F.; Kohse-Hoinghaus, K. *Catal. Commun.* **2009**, *11*(2), 118–122.
(11) Levasseur, B.; Kaliaguine, S. *Appl. Catal., A* **2008**, *343*(1−2), 29–38.
(12) Windisch, C. F.; Ferris, K. F.; Exarhos, G. J.; Sharma, S. K. *Thin Solid Films* **2002**, *420*, 89–99.
(13) Sehlin, S. R.; Anderson, H. U.; Sparlin, D. M. *Solid State Ionics* **1995**, *78*(3−4), 235–243.
(14) Bordeneuve, H.; Guillemet-Fritsch, S.; Rousset, A.; Schuurman, S.; Poulain, V. *J. Solid State Chem.* **2009**, *182*(2), 396–401.
(15) Douin, M.; Guerlou-Demourgues, L.; Menetrier, M.; Bekaert, E.; Goubault, L.; Bernard, P.; Delmas, C. *Chem. Mater.* **2008**, *20*(21), 6880–6888.
(16) Zhou, A. J.; Zhu, T. J.; Zhao, X. B. *Mater. Sci. Eng., B* **2006**, *128* (1−3), 174–178.
(17) Bialobok, B.; Trawczynski, J.; Mista, W.; Zawadzki, M. *Appl. Catal., B* **2007**, *72*(3−4), 395–403.
(18) Bahlawane, N.; Ngamou, P. H. T.; Vannier, V.; Kottke, T.; Heberle, J.; Kohse-Hoinghaus, K. *Phys. Chem. Chem. Phys.* **2009**, *11*(40), 9224–9232.
(19) Deng, J. G.; Zhang, L.; Dai, H. X.; He, H.; Au, C. T. *Ind. Eng. Chem. Res.* **2008**, *47*(21), 8175–8183.

Article

Chem. Mater., Vol. 22, No. 14, 2010 4159

2. Experimental Section

The growth of Co_3O_4 and $LaCoO_3$ thin films was performed in a cold-wall stagnation point-flow chemical vapor deposition (CVD) reactor, which is equipped with a pulsed-spray evaporation (PSE) system for the delivery of the liquid precursor feedstock. A schematic presentation of the deposition setup can be found elsewhere.[20] The total concentration of lanthanum and cobalt acetylacetonate in the feedstock was fixed at 10 mM and the La/Ca ratio was adjusted to obtain stoichiometric single-phase perovskite films. Both metal acetylacetonate precursors were dissolved in ethanol and kept at room temperature under atmospheric pressure during the growth. The pulsed-spray evaporation delivery was performed with an opening time of 2.5 ms and a frequency of 10 Hz. The injected feedstock was evaporated at 220 °C and the resulting vapor was transported to the deposition chamber with N_2/O_2 flow rates of 0.5/1 slm. Planar glass and mesh of stainless steel substrates were heated using a flat resistive heater. The temperature of the substrate was set at 400 °C, while the total pressure in the reactor was kept at 30 mbar during deposition. The thickness of the obtained films was estimated gravimetrically using a microbalance (Mettler ME30, digital resolution of 1 μg).

X-ray diffraction (XRD) patterns of the grown films were recorded at room temperature using a Phillips X'Pert Pro MDR diffractometer operated at 40 kV and 30 mA with a Cu Kα radiation. The crystalline phases were identified by referring to the powder XRD database (JCPDS-ICDD).

The optical absorption spectra of Co_3O_4 and $LaCoO_3$ thin films grown on glass substrates were obtained using a Shimadzu UV−vis spectrophotometer at room temperature in the 400 and 900 nm wavelength range. DC electrical resistivity measurements were performed in air atmosphere at temperatures in the range of 300−473 K using a PC-controlled four-probe equipment. The thermopower measurements were assessed using type-K thermocouples to measure the applied temperature gradient and platinum electrodes to measure the resulting voltages.

To investigate the surface reactivity, spinel Co_3O_4 or perovskite $LaCoO_3$ were grown as thin film on stainless steel mesh substrate and placed in a quartz reactor. The temperature-programmed reduction (TPR) by CO was carried out under 50 mL/min of argon containing 0.1% of CO, while the TPR by benzene, toluene, and *m*-xylene was assessed under 20 mL/min of argon flow containing around 1200 ppm of the aromatic volatile organic compound (VOC). The temperature was increased from 100 to 1000 °C with a ramp of 7 °C/min. The evolution of CO_2 ($m/z = 44$) for CO-TPR was monitored using a quadrupole mass spectrometer (Balzers QMG 112 A), while that of the aromatic VOCs was monitored by Fourier transform infrared spectroscopy (FTIR, Nicolet 5700) using a home-built transmission cell. All TPR tests were performed
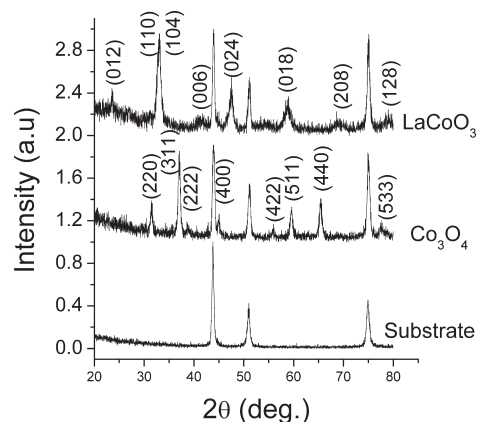

Figure 1. XRD patterns of $LaCoO_3$ and Co_3O_4 thin films grown on stainless steel mesh substrates at 400 °C.

at atmospheric pressure, and the obtained profiles were normalized to the mass and number of octahedrally co-ordinated cobalt cations per unit mass.

The catalytic activity toward the oxidation of alcohols (methanol, ethanol, *n*-propanol, and *n*-butanol), aromatic VOCs (*m*-xylene, toluene, and benzene), and CO was carried out at atmospheric pressure in a fixed-bed quartz reactor containing 5 mg of $LaCoO_3$ or Co_3O_4 in the form of thin films grown on mesh of stainless steel. For the evaluation of the catalytic activity, 30 mL/min of air containing 540 ppm of individual alcohols, 1200 ppm of aromatic VOCs, or 500 ppm of CO vapor was admitted to the reactor that corresponds to a gas hourly space velocity of 360 L g_{cat}^{-1} h^{-1}. The temperature was raised to 400 °C using a ramp of 2.6 °C/min, which accurately represents isothermal conditions. The temperature of the catalyst was monitored using a thermocouple that was in contact with the sample, while the exhaust gas composition was monitored by FTIR.

3. Results and Discussion

3.1. Structure. The structural characterization of spinel Co_3O_4 and perovskite $LaCoO_3$ thin films was performed using XRD and optical UV−visible absorption. The XRD patterns of the grown films of the stainless steel mesh substrates at 400 °C are presented in Figure 1. $LaCoO_3$ film exhibits a R-3C polycrystalline rhombohedral perovskite-type structure (PDF 48-0123), while Co_3O_4 films display a *Fd*3*m* polycrystalline cubic structure (PDF 42-1467). As far as the crystalline phases are concerned, the XRD analysis shows that the obtained films are pure phases of the spinel and of the perovskite. By applying the Debye−Scherrer formula to all observed diffraction peaks, the average crystallite size was estimated at (8.6 ± 0.8) nm for $LaCoO_3$ and (17.4 ± 1.1) nm for Co_3O_4 films. The growth of these materials with nanosized (< 20 nm) crystallites is typical for CVD-based processes.[21,22]

(20) Bahlawane, N.; Premkumar, P. A.; Onwuka, K.; Rott, K.; Reiss, G.; Kohse-Hoinghaus, K. *Surf. Coat. Technol.* **2007**, *201*(22−23), 8914–8918.

(21) Armelao, L.; Barreca, D.; Bottaro, G.; Gasparotto, A.; Maragno, C.; Tondello, E. *Chem. Mater.* **2005**, *17*(2), 427–433.
(22) Cheng, C. S.; Serizawa, M.; Sakata, H.; Hirayama, T. *Mater. Chem. Phys.* **1998**, *53*(3), 225–230.
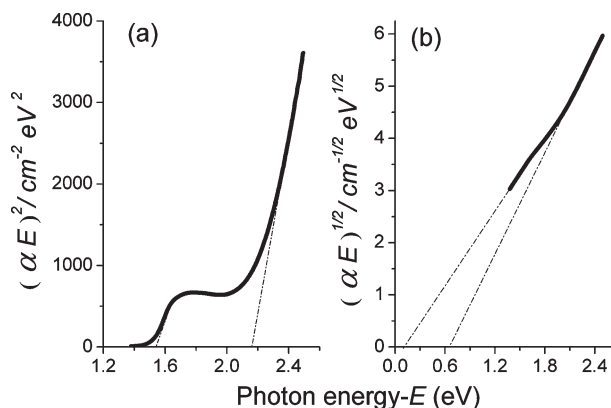
Figure 2. Tauc plots for Co_3O_4 (a) and $LaCoO_3$ (b) as a function of the photon energy.

Films of $LaCoO_3$ and Co_3O_4 with a thickness of 325 nm were grown on glass substrates for the optical characterization in the UV−visible range. Optical measurements have the advantage of involving both crystalline and amorphous phases and enable the determination of the band gap that is sensitive to the presence of defects and contaminations. Therefore, the optical characterization can be a valuable tool to confirm the purity of a crystalline structure. The absorption coefficients, α, were calculated from the measured absorbance of both films using the relation

$$\alpha = \frac{A \ln 10}{d} \qquad (1)$$

where A is the measured absorbance and d the thickness of the film. The band gap, E_g, for direct transitions is determined using the general formula[23]

$$\alpha E = \alpha_0 (E - E_g)^n \qquad (2)$$

where α_0 is a constant, E is the photon energy, and n is 1/2 for direct allowed transitions and 3/2 for direct forbidden transitions. The gap energy, E'_g, for indirect transitions is obtained from the following relation[24,25]

$$\alpha E = \alpha'_0 (E - E'_g \pm E_p)^n \qquad (3)$$

where α'_0 is a constant and n is 2 for indirect allowed transitions and 3 for indirect forbidden transitions. The +/− sign corresponds to phonon emission/absorption, and E_p is the energy of the involved phonon in the indirect transition of the electron. In the present study, the best fit of $(\alpha E)^{1/n}$ versus photon energy was obtained for $n = 1/2$ for Co_3O_4 and $n = 2$ for $LaCoO_3$. Figure 2a displays the $(\alpha E)^{1/2}$ versus E plot of a 325 nm-thick spinel cobalt oxide film, and two straight-line portions are obtained with intercepts at 1.52 (E_{opt1}) and 2.14 eV (E_{opt2}), suggesting the direct allowed transitions nature of these energies.
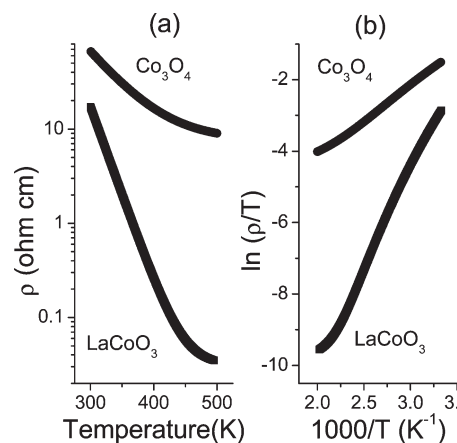

Figure 3. Temperature dependence (a) and Arrhenius plot (b) of the electrical resistivity for Co_3O_4 and $LaCoO_3$ films.

E_{opt1} is assigned to the charge transfer $O^{2-} \rightarrow Co^{3+}$, while E_{opt2} corresponds to the $O^{2-} \rightarrow Co^{2+}$ transition.[26] The values of E_{opt1} and E_{opt2} obtained in this study are in good agreement with those previously reported in the literature for Co_3O_4 films.[9,24−27] The $(\alpha E)^{1/2}$ versus E plot for the 325 nm-thick $LaCoO_3$ film is shown in Figure 2b, and two straight-line portions are observed with intercepts at 0.62 and 0.13 eV, leading to $E'_g = 0.37$ eV and $E_p = 0.25$ eV. The optical band gap (0.37 eV) of $LaCoO_3$ thin film obtained in this work agrees reasonably with the charge transfer O2p → Co3d gap (∼0.3 eV) reported by Arima et al.[28] using optical reflection spectroscopy for the $LaCoO_3$ bulk material.

In summary, the registered gap energies of the grown films are in good agreement with those previously reported for spinel Co_3O_4 and perovskite $LaCoO_3$ oxides. Therefore, the structural (XRD) and optical (UV−vis absorption) characterizations confirm the cubic-spinel structure of Co_3O_4 and the rhombohedral-perovskite nature of $LaCoO_3$ films and agree with the absence of amorphous contamination phases.

3.2. Electrical Transport Properties. The investigation of the transport properties of Co_3O_4 and $LaCoO_3$ films was performed using the temperature-programmed resistivity and Seebeck coefficient measurements.

3.2.1. Electrical Resistivity. The temperature dependence of the electrical resistivity (ρ) was measured for Co_3O_4 and $LaCoO_3$ films grown on glass substrates, the results of which are presented in Figure 3a. The electrical resistivity (ρ) of both oxides decreases with increasing temperature in the whole temperature range (300−473 K), showing the semiconductor-type behavior. However, the intriguing observation is the considerably more drastic decrease of the electrical resistivity of $LaCoO_3$ film (more than 2 orders of magnitude relative to Co_3O_4) upon the increase of the temperature. It is worth noting that an eventual oxygen deficiency in $LaCoO_3$ will result in an

(23) Kosacki, I.; Petrovsky, V.; Anderson, H. U. *Appl. Phys. Lett.* **1999**, *74*(3), 341–343.
(24) Patil, P. S.; Kadam, L. D.; Lokhande, C. D. *Thin Solid Films* **1996**, *272*(1), 29–32.
(25) Kadam, L. D.; Patil, P. S. *Mater. Chem. Phys.* **2001**, *68*(1−3), 225–232.
(26) Barreca, D.; Massignan, C.; Daolio, S.; Fabrizio, M.; Piccirillo, C.; Armelao, L.; Tondello, E. *Chem. Mater.* **2001**, *13*(2), 588–593.
(27) Yamamoto, H.; Tanaka, S.; Hirao, K. *J. Appl. Phys.* **2003**, *93*(7), 4158–4162.
(28) Arima, T.; Tokura, Y.; Torrance, J. B. *Phys. Rev. B* **1993**, *48*(23), 17006–17009.
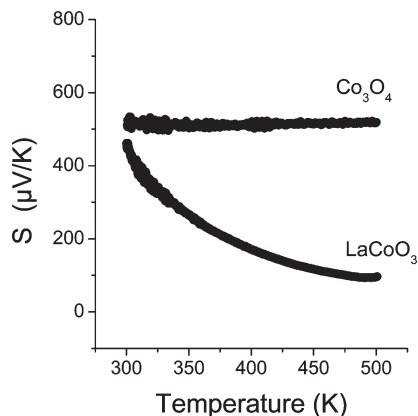
Figure 4. Temperature dependence of the Seebeck coefficient (S) of 325 nm-thick Co_3O_4 and $LaCoO_3$ films.

electron doping, which compensates the holes. Therefore, the presence of oxygen deficiency in $LaCoO_3$ can not explain its superior conductivity but rather induce its deterioration. In most oxides the electrical conduction is attributed to the "small-polaron mechanism", which involves the transport of localized charge states (small polaron) through the material.[12] Thus, the resistivity data for both oxides were fitted to the small-polaron-hopping model

$$\rho = AT \exp\left(\frac{E_a}{kT}\right) \quad (4)$$

where A is a pre-exponential factor, E_a is the apparent activation energy of conduction, k the Boltzmann constant, and T the absolute temperature. The plots of $\ln(\rho/T)$ versus $1/T$ of the samples in the range of 300−473 K, Figure 3b, exhibit a linear dependence. The experimental data diverge from the linearity at high temperature for $LaCoO_3$, which is a sign for the thermally activated percolation of the spin-ordering that gives the metallic conduction behavior.[29] The values of E_a calculated from the slope of the plots of Figure 3b are 0.17 and 0.48 eV for Co_3O_4 and $LaCoO_3$, respectively. E_a involves two contributions as attested by the following relation[16]

$$E_a = W_H + \frac{E_g}{2} \quad (5)$$

where W_H is the hopping energy and E_g is the gap energy, which is related to the concentration of the charge carriers. According to this relation, the observed difference between Co_3O_4 and $LaCoO_3$ in terms of electrical resistivity and apparent activation energy can be attributed either to the contrasting concentration of carriers and/or their mobility.

3.2.2. Thermoelectric Effect. The thermopower measurements were performed with the objective to identify the nature of the charge carriers and to provide an estimation of their concentration. The temperature dependence of the Seebeck coefficient (S) of Co_3O_4 and $LaCoO_3$ films is shown in Figure 4. The sign of the Seebeck

coefficient of $LaCoO_3$ and Co_3O_4 is positive in the measured temperature range (300−473 K), indicating that the dominant carriers are holes (Co^{4+} in the present case).

The thermopower of $LaCoO_3$ film drops significantly with increasing temperature as observed in Figure 4. This behavior indicates an increase of the concentration of holes due to the thermal activation. The estimation of C, the fraction of sites carrying the charge, can be obtained from Heikes' formula[30]

$$S - S_o = \frac{k}{e} \ln\left(\frac{1-C}{C}\right) \quad (6)$$

where k is the Boltzmann constant, e is the electronic charge, and S_o is generally neglected because its value is supposed to be less than 10 μV/K.[30] The application of eq 6 yields values of the fraction of charge carriers, C, of 4.8×10^{-3} to 0.245 when the temperature increases from 300 to 473 K. The gap energy (E_g) is obtained from the temperature-dependence of C according to the relation

$$C = C_0 \exp\left(\frac{-E_g}{2kT}\right) \quad (7)$$

where C_0 is a temperature-independent constant. From the Arrhenius plot of $\ln(C)$ versus $1/T$ (not shown here), a conductivity gap energy of 0.34 eV is obtained for $LaCoO_3$ film, which is close to the intrinsic gap energy reported by Dordor et al. (0.37 eV)[31] and Gerthsen et Hardlt (0.35 eV).[32] The conductivity gap energy almost coincides with the optical band gap (0.37 eV) obtained from Figure 2b, showing that the same energy states (O 2p and Co 3d) might be involved in the electron excitation. The hopping energy of $W_H = 0.31$ eV was calculated from eq 5.

The Seebeck coefficient of Co_3O_4, Figure 4, appears independent of the temperature, which is a strong indication that the fraction of charge carriers is constant. Its value was calculated to be $C = 1.4 \times 10^{-3}$ for the entire investigated temperature range. This observation agrees with the large gap energy (measured by absorption spectroscopy from Figure 2a) which cannot be overcome with the available thermal energy. Consequently, the decrease of the electrical resistivity with increased temperature (as shown in Figure 3a) can be only ascribed to the mobility of these holes. Therefore, the calculated apparent activation energy (0.17 eV) from Figure 3b corresponds to the hopping energy (W_H). This value agrees with the obtained 0.165 eV as hopping energy for a 650 nm thick Co_3O_4 film grown by CVD at a temperature of 550 °C.[22]

The remarkable difference in the calculated hopping energy for the perovskite (0.31 eV) and the spinel (0.17 eV) structures can be understood by considering the interconnection of octahedral sites in both oxides. As shown in

(29) Senaris-Rodriguez, M. A.; Goodenough, J. B. *J. Solid State Chem.* **1995**, *116*(2), 224–231.

(30) Raffaelle, R.; Anderson, H. U.; Sparlin, D. M.; Parris, P. E. *Phys. Rev. B* **1991**, *43*(10), 7991–7999.
(31) Dordor, P.; Joiret, S.; Doumerc, J. P.; Launay, J. C.; Claverie, J.; Hagenmuller, P. *Phys. Status Solidi A* **1986**, *93*(1), 321–328.
(32) Gerthsen, P.; Hardtl, K. H. *Z. Naturforsch. A* **1962**, *A 17*(6), 514–&.
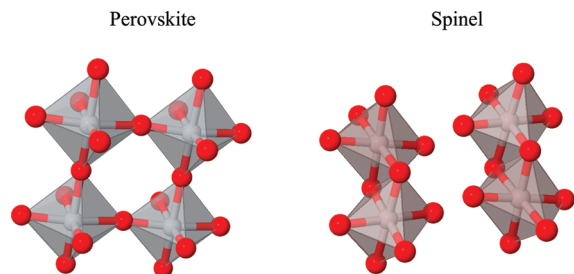
Perovskite   Spinel

Figure 5. Arrangement of the octahedrally coordinated sites in the spinel and perovskite oxides.

Figure 5, the adjacent octahedral sites in the perovskite are interconnected through their vertex (sharing one oxygen O^{2-} ion). The presence of oxygen forms an energetic barrier to the "hop" of the charge carrier between adjacent sites. In the spinel Co_3O_4 structure, however, adjacent octahedral sites are interconnected by their edges and consequently they share two O^{2-} ions. The coulomb repulsion between these two oxygen ions decreases the energetic barrier which facilitates the "hop" of the charge carrier.

Although, the interconnection geometry of the octahedral sites in the Co_3O_4 spinel structure favors the charge carrier hopping, the electrical conductivity remains inferior to that of the perovskite $LaCoO_3$. The creation of charge carriers occurs via a charge disproportionation between adjacent octahedrally coordinated trivalent cobalt cations.[33−37] This reaction depends inevitably on the way how these octahedra are arranged in respect to each others. The obtained experimental results show clearly that the equilibrium between the charge disproportionation and the charge coupling (reverse reaction) is at the favor of charge carrier creation in the structure with vertex-connected octahedra. Therefore, the great number of sites carrying the holes in $LaCoO_3$ largely offsets the high hopping energy.

3.3. Reducibility of $LaCoO_3$ and Co_3O_4 Films. The capacity of Co_3O_4 and $LaCoO_3$ to release their lattice oxygen upon the adsorption of reducing species was investigated using various probe molecules. The CO_2 evolution during the temperature-programmed reductions (TPR) with benzene, toluene, m-xylene and CO over $LaCoO_3$ and Co_3O_4 films is reported in Figure 6. The desorption of CO_2 during the redox reaction between the oxide and the reducing gases gives insight about the available types of oxygen, their relative abundance and their strength. Figure 6 shows TPR profiles that exhibit significant differences already at the first glance. It is worth mentioning that CO_2 was the only detected product of the redox reaction between the investigated oxides and the reducing
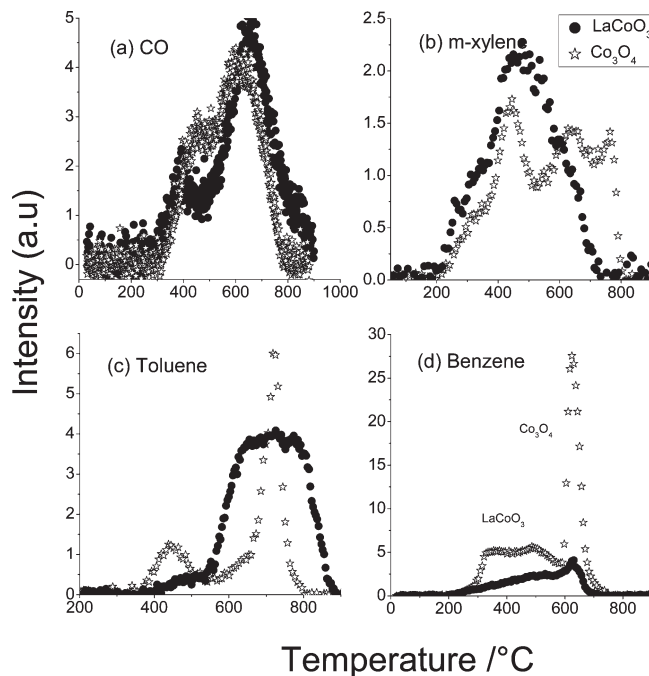

Figure 6. Profiles of CO_2 evolution during the TPR experiments.

probe molecules, which indicates that the further oxidation of the intermediates is faster than their desorption. The TPR profiles of Co_3O_4 and $LaCoO_3$ in Figure 6a reveal the presence of two components even with CO as the simplest probe molecule. The ex situ XRD analysis after TPR tests, see Supporting Information, shows that no metallic cobalt forms even after reduction at 900 °C with CO, which contrasts with the H_2-TPR.[9,38] The high lability of the lattice oxygen in Co_3O_4 leads to reactions at the surface and at the interface. At the surface, CO is oxidized and consequently CoO forms. This reaction competes with that occurring at the interface. The reaction at the interface leads to the formation of $CoFe_2O_4$, which the lattice oxygen is less labile.[18] The reduction of the iron-containing spinel takes place at higher temperature leading to the second TPR peak.

The lattice oxygen in $LaCoO_3$ reacts also at both boundaries. At the surface, CO is oxidized and the perovskite became oxygen-deficient as clearly shown in the XRD analysis (Supporting Information). This results agrees with the H_2-TPR reported by Ivanova et al.[38] The reaction at the interface produces iron oxide, which is reduced at higher temperature, where the oxygen-deficient perovskite collapses to form La_2O_3 and CoO.

Considering the increased complexity due to the interfacial reaction, the comparison of the TPR profiles is limited to temperatures lower than 450 °C. Within this temperature range, probing the surface with CO shows that, relative to $LaCoO_3$, Co_3O_4 presents a slightly higher lattice oxygen lability. The more complex probe molecules (see Figure.6 b-d) show in addition to the components at

(33) Tealdi, C.; Malavasi, L.; Fisher, C. A. J.; Islam, M. S. *J. Phys. Chem. B* **2006**, *110*(11), 5395–5402.
(34) Petrov, A. N.; Zuev, A. Y.; Vylkov, A. I.; Tsvetkov, D. S. *J. Mater. Sci.* **2007**, *42*(6), 1909–1914.
(35) Brabers, V. A. M.; Broemme, A. D. D. *J. Magn. Magn. Mater.* **1992**, *104*, 405–406.
(36) Lenglet, M.; Jorgensen, C. K. *Chem. Phys. Lett.* **1994**, *229*(6), 616–620.
(37) Douin, M.; Guerlou-Demourgues, L.; Menetrier, M.; Bekaert, E.; Goubault, L.; Bernard, P.; Delmas, C. *J. Solid State Chem.* **2009**, *182*(5), 1273–1280.

(38) Ivanova, S.; Senyshyn, A.; Zhecheva, E.; Tenchev, K.; Nikolov, V.; Stoyanova, R.; Fuess, H. *J. Alloys Compd.* **2009**, *480*(2), 279–285.
(39) Tejuca, L. G.; Bell, A. T.; Fierro, J. L. G.; Pena, M. A. *Appl. Surf. Sci.* **1988**, *31*(3), 301–316.
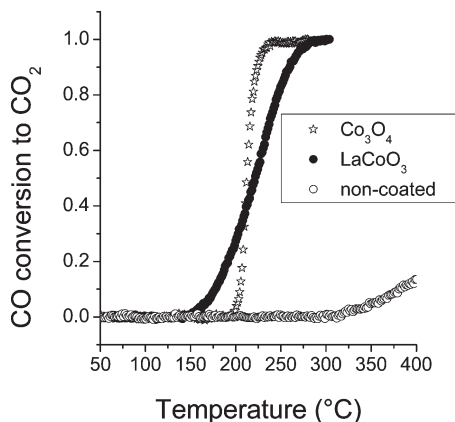
Figure 7. Light-off curves of the catalytic combustion of CO over the noncoated stainless steel mesh and the coated ones with Co_3O_4 and $LaCoO_3$.

~400 °C and ~600 °C a component at ~300 °C with m-xylene and benzene; ~ 500 °C with benzene and > 700 °C with toluene and m-xylene. Each component might correspond to a reaction step either at the interface or at the surface of the oxide layer. The identification of these reactions steps requires a thorough investigation with surface-sensitive vibrational spectroscopy, a study that is beyond the scope of the present work.

The use of CO, toluene, and benzene as probe molecules illustrates clearly, at least at low temperature, the higher reducibility of the edge connected octahedrally coordinated Co^{3+} (Co_3O_4) relative to the vertex connected ones ($LaCoO_3$).

3.4. Surface Reactivity. The surface reactivity of Co_3O_4 and $LaCoO_3$ films was tested toward the catalytic oxidation of CO, aromatic compounds (benzene, toluene, and m-xylene) and alcohols (methanol, ethanol, n-propanol, and n-butanol). The oxidation of the chosen compounds was considered for the comparative study of the surface reactivity of $LaCoO_3$ and Co_3O_4 relative to their structure.

3.4.1. CO Combustion. The CO catalytic combustion over Co_3O_4 and $LaCoO_3$ exhibits significant differences in terms of onset and steepness of the light off curve as shown in Figure 7. Relative to the spinel oxide, the observed onset temperature and the curve steepness are significantly lower for the CO oxidation reaction over the perovskite oxide. It is worth noting that the temperatures corresponding to the total oxidation of CO over both oxides (241 °C for Co_3O_4 and 285 °C for $LaCoO_3$) are below the temperature of CO_2 evolution (310 °C) during the CO-TPR experiments. Therefore it can be concluded that the bulk lattice-oxygen is unlikely to be involved for the total oxidation of CO, which means that the addressed reaction follows a suprafacial mechanism where the adsorbed oxygen allows the total oxidation of CO.[39]

The abundance of the surface oxygen depends on the electron acceptor character of the octahedrally coordinated cobalt at the surface. Consequently, the presence of
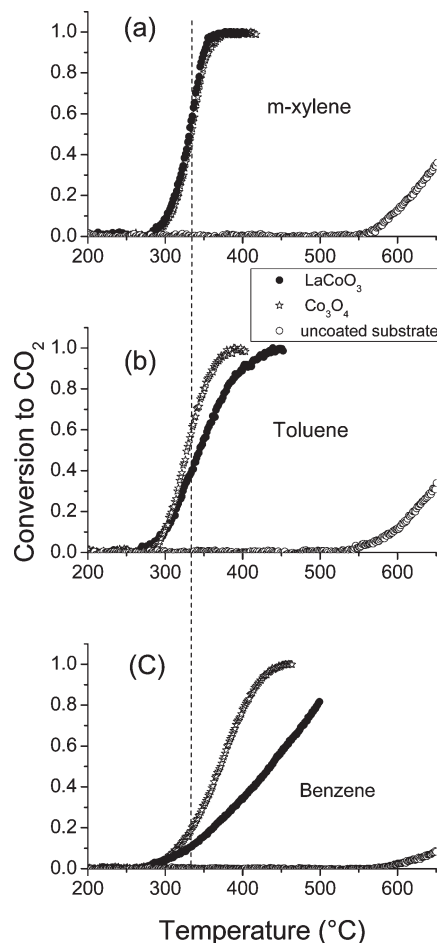

Figure 8. Light-off curves of the catalytic combustion of aromatic compounds over the noncoated stainless steel mesh and the coated ones with Co_3O_4 and $LaCoO_3$.

tetravalent cobalt in the octahedral site, the hole carrying the electrical charge, is expected to promote the adsorption of oxygen at the surface of $LaCoO_3$ films.[40] Therefore, the abundance of the charge carriers in the perovskite structure, Figure 4, is probably responsible for the observed lower onset temperature. The difference in the steepness of the light off curves is related to the strength of the oxygen binding to the surface.

3.4.2. Combustion of Aromatic Volatile Organic Compounds. Figure 8 shows the activity of Co_3O_4 and $LaCoO_3$ films for the oxidation of aromatic compounds at a concentration of 1200 ppm. It is noteworthy that all investigated hydrocarbons are completely converted to CO_2 at temperatures that are below the reaction onset over the noncoated support. As clearly depicted in Figure 8, the catalytic activity of both oxides decreases according to the order of m-xylene > toluene > benzene. The observed trend can be explained by the difference of the strength of the weakest C−H bond expressed by means of bond dissociation enthalpy, which increases from m-xylene (377 kJ/mol) to toluene (1549 kJ/mol) and benzene (1946.8 kJ/mol).[41,42] Thus, the presence of the methyl group in the

(40) Ngamou Tchoua, P. H.; Kohse-Höinghaus, K.; Bahlawane, N. *J. Appl. Phys.* **2009**, *106*, 073714.

(41) Alifanti, M.; Florea, M.; Parvulescu, V. I. *Appl. Catal., B* **2007**, *70* (1−4), 400–405.

(42) Hammad, L. A.; Wenthold, P. G. *J. Am. Chem. Soc.* **2000**, *122*(45), 11203–11211.
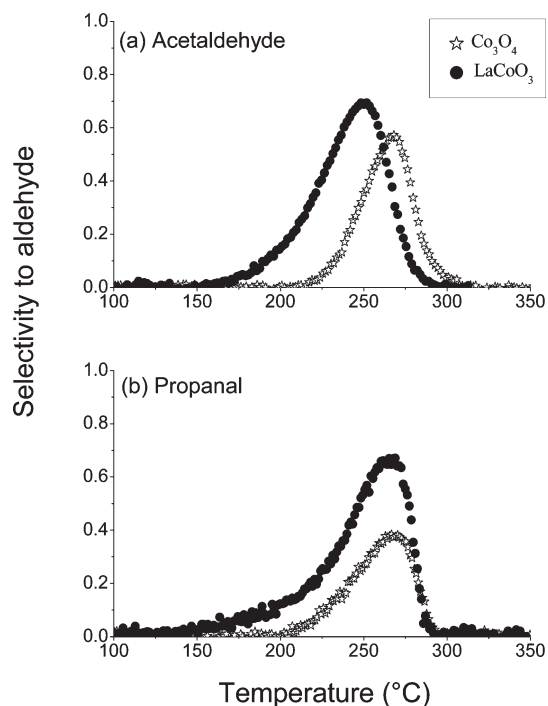
Figure 9. Catalytic partial oxidation of ethanol (a) and *n*-propanol (b) to the corresponding aldehydes over Co_3O_4 and $LaCoO_3$ coated stainless steel mesh substrates as a function of the temperature.
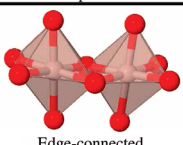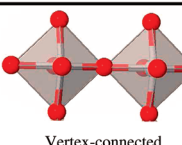
Table 1. Overview of the Structure−Properties−Reactivity Interplay in Octahedrally Coordinated Co^{3+} Cations

aromatic ring allows the fast activation of the C−H bond at low temperature.

As shown in Figure 8a, the deep oxidation of m-xylene does not seem to be an appropriate reaction to illustrate the difference between Co_3O_4 and $LaCoO_3$. The slightly higher reducibility of the perovskite by m-xylene, Figure 6b, does not correlate with the combustion performance. The fact that the catalytic combustion of *m*-xylene is insensitive to the noticed difference in the redox properties of both oxides indicates that the uptake of the lattice oxygen is not the rate-limiting step.

The results in Figure 8b−c show that the activity of the spinel Co_3O_4 outperforms that of the perovskite $LaCoO_3$ for the oxidation of benzene, and toluene to a lesser extent. This result is in agreement with the observed low-temperature release of the lattice oxygen in the benzene- and toluene-TPR profiles in Figure 6, confirming that the reduction of the octahedrally coordinated Co^{3+} ions to Co^{2+} plays a relevant role for the total oxidation of aromatics. In fact, this reduction reaction supplies the necessary oxygen for the oxidation of the hydrocarbons. The reoxidation occurs via the uptake of oxygen from the gas phase. The overall described mechanism corresponds to the Mars-van Krevelen (MVK) kinetics, which involves the reduction−oxidation cycle of the catalyst surface.

The effect of the higher reducibility of the edge-connected octahedrally coordinated Co^{3+} (Co_3O_4) relative to the vertex-connected ones ($LaCoO_3$) is clearly illustrated by the improved catalytic efficiency toward the oxidation of toluene and benzene (Figure 8b and c). In fact, these reactions are sensitive to the amount of the released lattice oxygen by $LaCoO_3$ and Co_3O_4 as attested by the corresponding TPR profiles (Figure 6c and d).

3.4.3. Alcohol Oxidation. The catalytic activity of the spinel Co_3O_4 and the perovskite $LaCoO_3$ thin films toward the oxidation of methanol, ethanol, *n*-propanol, and *n*-butanol was investigated. These alcohols are completely converted to CO_2 starting at 300 °C that is below the reaction onset over noncoated supports. Except for methanol which is directly converted to CO_2, the oxidation of the higher alcohols occurs through the formation of the corresponding aldehydes at intermediate temperatures as shown for ethanol and *n*-propanol in Figure 9. Regarding the catalytic selective oxidation of alcohols to form aldehydes, the illustrated examples in Figure 9 show clearly that the perovskite exhibits a higher efficiency relative to the spinel.

The partial oxidation of alcohols requires the presence of basic sites to allow the deprotonation (H-abstraction) of the adsorbed alkoxide species. Therefore, probing the surface basicity with ethanol and *n*-propanol reveals higher strength and abundance of the basic sites in $LaCoO_3$ relative to Co_3O_4 since lower onset temperatures and higher selectivity values are observed.

The formation of basic sites results from the adsorption of gas phase oxygen, which is promoted by the presence of tetravalent cobalt cations, Co^{4+}, at the surface. Therefore, the higher activity of the perovskite can be attributed to the demonstrated, Figures 3 and 4, higher concentration of the charge carriers (Co^{4+}), which is related to the arrangement of the cobalt octahedral sites.

The correlation between the electrical charge transport and the surface basicity, expressed in terms of selective conversion of ethanol to acetaldehyde was also previously proposed for the spinel[18] using a doping strategy. Furthermore, a recent study has clearly shown that the electrical charge transport in $LaCoO_3$ ultrathin films is overwhelmed by the surface contribution, which is due to the adsorption of the gas phase oxygen.[40] The latter was shown to be responsible for the stabilization of the charge carriers (Co^{4+}) at the surface of $LaCoO_3$.

4. Conclusion

Co_3O_4 and $LaCoO_3$ films have been grown using pulsed-spray evaporation chemical vapor deposition method and the presence of pure rhombohedral perovskite and cubic spinel structures was confirmed by XRD and optical absorption UV−visible measurements. The electrical measurements reveal that the hopping of the small-polaron, which takes place in the octahedral sites, drives the electrical transport in both oxides. The intriguing superior electrical conductivity of $LaCoO_3$ films relative to Co_3O_4 is attributed to the high concentration of the charge carriers (Co^{4+}), which is the result of the favorable charge disproportionation between trivalent cobalt cations in vertex-connected octahedra.

The higher reducibility of the edge-connected octahedrally coordinated Co^{3+} (Co_3O_4) relative to the vertex-connected ones ($LaCoO_3$) is found to be responsible for the superior activity of Co_3O_4 toward the deep oxidation of aromatic compounds. However, the performance gap between both structures is significantly influenced by the ability of the aromatic compounds to accept the anionic lattice oxygen.

In contrast to the oxidation of aromatic compounds, the oxidation of CO involves a suprafacial mechanism related to the presence of surface tetravalent cobalt cations. The latter are also related to the abundance and the strength of the surface basic sites, which determine the efficiency of the oxides as partial oxidation catalysts. A summary of the experimentally demonstrated differences between the edge- and the vertex-connected octahedrally coordinated Co^{3+} is given in Table 1.

Supporting Information Available: Ex situ XRD study of the CO-reduced cobalt oxides and a short discussion. This material is available free of charge via the Internet at http://pubs.acs.org.